fractal and fractional

MDPI

Article

The Impact of Fractal Gradation of Aggregate on the Mechanical and Durable Characteristics of Recycled Concrete

Chang-Qing Quan [1], Chu-Jie Jiao [1,*], Wei-Zhi Chen [1], Zhi-Cheng Xue [2], Rui Liang [3] and Xue-Fei Chen [1,4,*]

[1] School of Civil Engineering, Guangzhou University, Guangzhou 510006, China; 2112116013@e.gzhu.edu.cn (W.-Z.C.)
[2] Architecture and Civil Engineering Institute, Guangdong University of Petrochemical Technology, Maoming 525000, China
[3] Zhuhai UM Science &Technology Research Institute, Zhuhai 519031, China
[4] Joint Key Laboratory of the Ministry of Education, Institute of Applied Physics and Materials Engineering, University of Macau, Avenida da Universidade, Taipa, Macau SAR 999078, China
* Correspondence: cejiaochujie@gzhu.edu.cn (C.-J.J.); chenxuefei@gzhu.edu.cn (X.-F.C.)

Abstract: Properties of recycled aggregate concrete (RAC) are influenced by the composition and particle size distribution of recycled coarse aggregate (RCA). The study herein designed seven distinct groups of RACs with varying aggregate fractal dimensions (***D***) and one group of natural concrete (NAC). The impact of ***D*** on the workability, compressive strength, resistance to chloride ion penetration, and carbonation resistance of RAC was measured. It was found that an increase in the D value led to a decrease in the slump and slump flow, with the compressive strength and chloride ion penetration increasing and then decreasing, and carbonation gradually declined. The optimal fractal dimension was thereby determined to be 2.547 by a strength model accommodating two parameters of ***D*** and the curing age. Additionally, the mass percentage of each particle size for the corresponding gradation was presented. The compressive strength and chloride permeation resistance of RAC (***D*** = 1.0) relative to RAC (***D*** = 2.5) was increased by 16.7% and 13.3%, respectively. Furthermore, the carbonation depth of RAC (***D*** = 2.5) was comparable to that of NAC. Additionally, the carbonation resistance of RAC was influenced by both the size distribution and the degree of natural carbonation of RCA, resulting in four distinct features relative to NAC. It is thereby feasible to enhance RAC performance through the manipulation of RCA's fractal dimensions.

Keywords: aggregate fractal gradation; recycled aggregate; compressive strength; chloride ion permeability; carbonation resistance

Citation: Quan, C.-Q.; Jiao, C.-J.; Chen, W.-Z.; Xue, Z.-C.; Liang, R.; Chen, X.-F. The Impact of Fractal Gradation of Aggregate on the Mechanical and Durable Characteristics of Recycled Concrete. *Fractal Fract.* **2023**, *7*, 663. https://doi.org/10.3390/fractalfract7090663

Academic Editor: Wojciech Sumelka

Received: 6 July 2023
Revised: 22 August 2023
Accepted: 30 August 2023
Published: 31 August 2023

1. Introduction

The construction, renovation, and demolition of buildings and structures worldwide generates large amounts of construction and demolition waste (C&DW) [1]. In China alone, up to 3.5 billion tons of C&DW are generated annually, with the majority being waste concrete [2]. Disposing of waste concrete in landfills can have a substantial negative impact on the surrounding environment. Thus, researchers are exploring alternative disposal approaches, such as recycling and reusing, particularly because China consumes about 20 billion tons of natural coarse aggregates (NCA) per year. Numerous studies have been carried out on RAC, including investigations into its properties and composition by Tang et al. [3], modifications with basalt fibers by Xiong et al. [4], mechanical properties and microscopic pore structure by Xu et al. [5], water absorption and resistance to chloride ion erosion by Bao et al. [6], and seismic performance of RAC structures by Silva et al. [7]. Despite these efforts, the limited workability, low strength, poor durability, and unstable performance of RAC continue to hinder its widespread use in engineering applications.

The negative characteristic of RAC is attributed to the presence of residual cementitious material within the porous old mortar of the RCA. To address this issue, two primary

approaches have been explored to mitigate the negative impact of RCA on the properties of RAC. These approaches involve enhancing the properties of RA and incorporating admixtures. There exist two primary approaches for enhancing the quality of RCA: first, the removal of the hardened cement mortar from the RCA surface can be achieved through the utilization of methods such as heating, aggregate shaping, and acid immersion; second, the reinforcement of the hardened cement mortar on the RCA surface can be accomplished through techniques such as polymer emulsion immersion, volcanic ash slurry impregnation, calcium locking, and adjustment of the mixing method. According to Ryu et al. [8], the utilization of aqueous H_2SiF_6 solution can enhance the density and diminish the water absorption of RCA. Additionally, the compressive strength of RAC treated with aqueous H_2SiF_6 solution exhibits a marginal increase in comparison to untreated RAC. Tang et al. [9] employed a lithium silicate solution to reinforce the surface of RCA and reported that this treatment can enhance the strength of the interfacial transition zone (ITZ) between the old and new mortar. Nevertheless, the elastic modulus did not exhibit a discernible increase. Notably, the presence of residual chloride and sulfate ions on the RCA surface following acid immersion may compromise the long-term properties of RAC, particularly its durability. Furthermore, the disposal of waste liquid poses a significant challenge. Kou and Poon [10] discovered that the incorporation of RCA in polyvinyl alcohol (PVA) can enhance the mechanical characteristics and chloride ion resistance of RAC. Subsequently, it was observed that the application of silane-based water repellent can enhance the durability of RAC, but will reduce its compressive strength [11]. Santos et al. [12] demonstrated that silane penetrates pores smaller than 100 nm, whereas paraffin infiltrates pores larger than 100 nm.

Due to its hydrophobic nature, the polymer slurry tends to persist on the surface of recycled concrete aggregate (RCA) after immersion treatment. This residue infiltrates into the fresh mortar during mixing, impeding the interaction between cement and water and consequently hindering cement hydration. As a result, there is a potential for decreased strength in recycled aggregate concrete (RAC). To avoid this issue, previous research [13,14] has employed pozzolanic slurry for RCA immersion. Ultrafine pozzolanic powders have the ability to infiltrate the cracks of RCA and react with $Ca(OH)_2$ in RCA, resulting in the formation of C-S-H gel. This process can enhance the internal microstructure of RCA and subsequently improve its performance. In addition, Wang et al. [15] and Feng et al. [16] have utilized microorganisms to carbonize RCA, which has been found to enhance the compressive strength and reduce water absorption of RAC. Shi et al. [17–19] and Pan et al. [20] utilized high concentrations of CO_2 to carbonize RCA, resulting in favorable outcomes. Li et al. [21] and Kong et al. [22] employed two-stage and three-stage mixing methods, respectively, to prepare RAC, which contributed to the enhancement of compressive strength. Kou and Poon [23] determined that the addition of external admixture of 25% and 35% fly ash effectively mitigates the detrimental effects of RCA, but the substitution of an equivalent amount of cement with fly ash decreases the compressive strength of RAC.

The aforementioned studies center on enhancing and refining the composition of RCA. It is noteworthy that concrete exhibits self-similar fractal properties [24–26], and the utilization of fractal theory as a means to investigate concrete properties is increasingly appealing [27–30]. The microstructure of concrete, encompassing porosity, hydration products, aggregate distribution, and cracks, may be regarded as possessing fractal attributes [31]. Wang et al. [32–34] developed a fractal sponge model to investigate the relationship between properties, including porosity, permeability, pore structure and fractal dimension. Prior studies have established the noteworthy influence of aggregate morphology on the properties of concrete [35–37]. The assessment of this morphology can be accomplished through the measurement of fractal dimension [38], with aggregate particle size serving as a defining feature of aggregate morphology. Akbarnezhad et al. have identified a substantial association between the mortar content, apparent density, and water absorption of RCA and aggregate particle size [39]. It is clear that the size of the aggregate is closely related to the gradation, and the gradation distribution of RCA can provide insight into the content

of adhering old mortar. Consequently, the present study endeavors to investigate the correlation between the fractal gradation of RCA and the performance of RAC.

The primary aim of this research is to examine the impact of RCA fractal gradation on the workability, compressive strength, and durability of RAC. Initially, the fractal gradation was introduced and the formula for the passing rate of each sieve size was derived, followed by the calculation of gradation curves for seven different fractal dimensions. Subsequently, seven distinct groups of RAC with varying fractal dimensions and one group of NAC were designed, and the RAC was mixed by four additions. After curing under standard conditions to the prescribed age, the compressive strength, total charge passed, and carbonation depth were measured, and the impact of fractal dimension on the aforementioned performance of RAC was analyzed.

2. Materials and Methods

2.1. Materials

2.1.1. Cement

The RAC was prepared using P·II 42.5R Portland cement produced by China Resources Cement Holdings Limited, which exhibited an apparent density of 3120 kg/m^3 and a specific surface area of 359 m^2/kg. Table 1 presents additional physical and mechanical characteristics of the cement.

Table 1. The primary characteristics of P·II 42.5R.

Loss (%)	Stability	Setting Time (min)		Compressive Strength (MPa)			Flexural Strength (MPa)		
		Initial	Final	3 d	7 d	28 d	3 d	7 d	28 d
2.0	Qualified	125	230	28.3	37.5	46.2	5.7	6.8	7.9

2.1.2. Fly Ash and Slag

Equal amounts of Grade II fly ash and S95 slag were utilized as cement substitutes to mitigate carbon emissions during concrete preparation and enhance its subsequent performance. The chemical and physical characteristics of fly ash and slag are presented in Tables 2 and 3, respectively.

Table 2. The chemical constitution of fly ash and slag.

Materials	SiO_2	Al_2O_3	CaO	Fe_2O_3	Na_2O	MgO	K_2O	TiO_2	P_2O_5	SO_3	Loss
Fly ash	45	36.5	5.74	6.15	0.46	0.8	1.19	1.66	0.31	0.79	1.4
Slag	36.2	18.9	32.29	4.53	0.36	1.54	0.56	3.36	0.25	1.52	0.49

Table 3. The physical properties of fly ash and slag.

Materials	Apparent Density (kg/m^3)	Specific Surface Area (m^2/kg)	Compressive Strength (MPa)			Activity Index (%)		
			7 d	28 d	60 d	7 d	28 d	60 d
Fly ash	2200	325	25.7	42.5	46.2	67.4	92.3	96.2
Slag	2900	378	26.9	44.4	49.2	70.8	96.6	102.5

2.1.3. Coarse Aggregate

A proportion of NCA and RCA was used as coarse aggregate in the concrete mix. The NCA was obtained from a local commercial concrete company and comprised crushed granite. The RCA, on the other hand, was derived from waste concrete that underwent crushing by a crawler mobile crusher, resulting in continuously graded particles that conformed to the specifications outlined in the Current Chinese National Standard "Recycled Coarse Aggregate for Concrete". The crushing indices of RCA and NCA are 8.6% and

12.5%, respectively. Additionally, Figure 1 illustrates the bulk density, apparent density, and water absorption of NCA and RCA. As depicted in the figure, the density of RCA is inferior to that of NAC, whereas the water absorption of RCA is superior to that of NCA. The apparent density of RCA exhibits an increase with an increase in particle size, whereas the apparent density of NAC remains largely unaffected by particle size. This phenomenon can be attributed to a decrease in the amount of old mortar adhering to RCA per unit volume as particle size increases, leading to an increase in mass and apparent density. Additionally, the water absorption of RCA decreases with the increase of particle size, with a reduction rate significantly greater than that observed for NCA. Hence, the particle size distribution represents a crucial parameter in determining the characteristics of RCA, which may significantly affect the performance of RAC. Therefore, it is imperative to conduct research in this area.

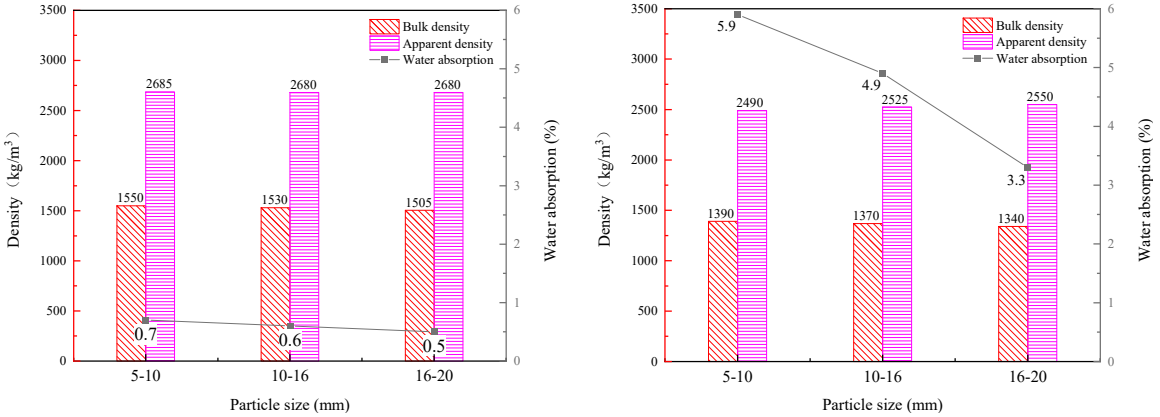

(**a**) NCA (**b**) RCA

Figure 1. The bulk density, apparent density, and water absorption of coarse aggregate.

2.1.4. Fine Aggregate

A particular ratio of river sand and manufactured sand was employed as the fine aggregate. The apparent density and fineness modulus of the river sand were measured as 2520 kg/m^3 and 2.7, respectively, whereas the manufactured sand demonstrated an apparent density and fineness modulus of 2580 kg/m^3 and 2.9, respectively.

2.1.5. Water and Water Reducer

In this study, the naphthalene plasticizer was employed as a water reducer to mitigate the adverse impact of water absorption on the workability of RCA. The characteristics and performance of the water reducer are presented in Table 4, while tap water was utilized as the mixing water.

Table 4. The properties of plasticizer.

Properties	Solid Content (%)	pH Value	Specific Gravity	Water Reduction Rate (%)	Cl^- Content (mg/L)
Results	5.2	6.82	1.024	12.5%	3.2

2.2. Fractal Dimension of Aggregate

Prior research has demonstrated that the performance of RCA may be notably impacted by its particle size [39]. Therefore, it is imperative to ascertain the mass proportion of each particle size. If the aggregate particles are arranged by particle size intervals and the number of particles in each particle size interval is counted, it is clear that the aggregate set has the fractal properties of statistical self-similarity. In addition, the aggregate also accords with the condition of fractal characteristics in shape, so the theory of fractal geometry can

be used to describe the gradation distribution of aggregate. In the following paper, the mass distribution function of the fractal gradation of RCA gradation is derived using fractal theory.

For fractal bodies, any fractal indicator can be calculated by the following formula

$$\boldsymbol{Z} = \boldsymbol{Z}_0 \times \boldsymbol{\lambda}^{\boldsymbol{E}-\boldsymbol{D}} \tag{1}$$

where $\boldsymbol{Z}$ is the indicator of the fractal body; $\boldsymbol{Z}_0$ is the indicator when $\boldsymbol{E} = \boldsymbol{D}$; $\boldsymbol{Z}$ corresponds to the number of points, length, area, and volume when $\boldsymbol{E}$ is 0, 1, 2, and 3, respectively; $\boldsymbol{D}$ is the value of fractal dimension, while $\boldsymbol{\lambda}$ is the dimensionless yardstick length, which can be calculated using the following formula.

$$\boldsymbol{\lambda} = \boldsymbol{\delta} / \boldsymbol{\delta}_{\max} \tag{2}$$

where $\boldsymbol{\delta}$ represents the dimensioned yardstick length, which is constrained by the inequality $\boldsymbol{\delta}_{\min} \leq \boldsymbol{\delta} \leq \boldsymbol{\delta}_{\max}$.

The set of aggregates depicted in Figure 2 is partitioned into n grades based on particle size, where the quantity of aggregates in each grade is denoted as $\boldsymbol{n}_{\mathrm{i}}$ (i = 1, 2, 3, . . ., n). It is evident that:

$$\sum_{i=1}^{n} \boldsymbol{n}_i = \boldsymbol{N}_0 \tag{3}$$

where $\boldsymbol{N}_0$ is the aggregate count within the gradation set and is constant for a given gradation set.

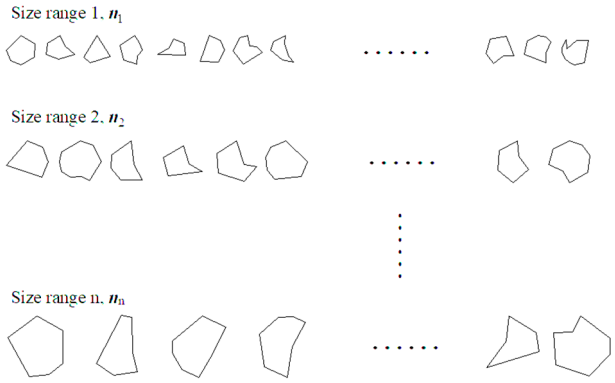

Figure 2. Schematic diagram of size classification of aggregate gradation.

If $\boldsymbol{E} = 0$, Formula (1) is written as

$$\boldsymbol{N}(\boldsymbol{r}) = \boldsymbol{N}_0 \times (\boldsymbol{r}/\boldsymbol{r}_{\max})^{-\boldsymbol{D}} \tag{4}$$

where $\boldsymbol{r}$ is the aggregate particle size; $\boldsymbol{N}(\boldsymbol{r})$ denotes the cumulative count of aggregates with a diameter that does not exceed $\boldsymbol{r}$, and $\boldsymbol{D}$ signifies the fractal dimension of the aggregate particle size distribution.

Since $\boldsymbol{r}_{\max}$ and $\boldsymbol{D}$ are constants, to facilitate the calculation, Formula (4) is rewritten as

$$\boldsymbol{N}(\boldsymbol{r}) = \frac{\boldsymbol{N_0}}{\boldsymbol{r}_{\max}^{-\boldsymbol{D}}} \times \boldsymbol{r}^{-\boldsymbol{D}} = \boldsymbol{H}\boldsymbol{r}^{-\boldsymbol{D}} \tag{5}$$

The relationship between mass and volume is

$$d\boldsymbol{M}(\boldsymbol{r}) = \boldsymbol{\rho}\boldsymbol{V}(\boldsymbol{r})\, d\boldsymbol{N}(\boldsymbol{r}) \tag{6}$$

where ρ represents the density of the aggregate while $d\boldsymbol{M}(\boldsymbol{r})$ and $d\boldsymbol{N}(\boldsymbol{r})$ denote the cumulative mass and accumulated number of aggregates, respectively. Within the particle size

interval [r, $r + dr$], $V(r)$ is the volume of a single aggregate, which is calculated by the following formula.

$$\boldsymbol{V(r) = \beta r^3} \tag{7}$$

where $\boldsymbol{\beta}$ is the volume shape factor of the aggregate.

The cumulative mass($\boldsymbol{M(r)}$) of aggregates with a diameter not larger than $\boldsymbol{r}$ can be obtained by calculating (5) to (7) jointly

$$\boldsymbol{M(r) = -\frac{\rho\beta HD}{3-D} r^{3-D}} + \mathrm{C} \tag{8}$$

where **C** is an integral constant.

When $\boldsymbol{r}$ is designated as $\boldsymbol{r}_{\min}$, the quantity of aggregates at these dimensions is minimal and inconsequential in relation to the overall quantity of aggregates within the system, so $\boldsymbol{M}(\boldsymbol{r}_{\min})$ is 0; when r is taken as $\boldsymbol{r}_{\max}$, $\boldsymbol{M}(\boldsymbol{r}_{\max})$ represents the entire mass of the aggregate system, denoted as $\boldsymbol{M_0}$.

$$\begin{cases} \boldsymbol{M(r_{min}) = 0} \\ \boldsymbol{M(r_{max}) = M_0} \end{cases} \tag{9}$$

By substituting Formula (9) into Formula (8), the following can be obtained:

$$\begin{cases} \boldsymbol{-\frac{\rho\beta HD}{3-D} = \frac{M_0}{r_{max}^{3-D} - r_{min}^{3-D}}} \\ \mathrm{C} = \boldsymbol{-\frac{M_0}{r_{max}^{3-D} - r_{min}^{3-D}} r_{min}^{3-D}} \end{cases} \tag{10}$$

And Formula (8) can be written as

$$\boldsymbol{M(r) = \frac{r^{3-D} - r_{min}^{3-D}}{r_{max}^{3-D} - r_{min}^{3-D}} M_0} \tag{11}$$

Define the mass distribution function ($\boldsymbol{P(r)}$) of aggregate:

$$\boldsymbol{P(r) = \frac{M(r)}{M_0} = \frac{r^{3-D} - r_{min}^{3-D}}{r_{max}^{3-D} - r_{min}^{3-D}}} \tag{12}$$

Formula (12) enables the computation of the passage rate of each sieve pore within the particle size range [$r_{\min}$, $r_{\max}$] given a fixed fractal dimension of the aggregate.

The present investigation considers a continuous gradation range of NCA and RCA within the 5–20 mm range. The passing rate for each sieve pore, characterized by fractal dimensions of 1.0, 1.5, 2.4, 2.5, 2.6, 2.7, and 2.8, was determined using Formula (12) and is presented in Figure 3. The resulting data were then converted into mass proportions for each particle size range, as summarized in Table 5. As shown in Figure 3, there is a one-to-one correspondence between the aggregate fractal dimension and the gradation curve. In other words, for a given fractal dimension, there exists a corresponding gradation curve, which is referred to as the fractal gradation curve.

2.3. Mixture Proportion

The Chinese industrial standard "Specification for mix proportion design of ordinary concrete" was employed to determine the mixture proportion of reference and experimental concrete using the absolute volume method. The study utilized a water–binder ratio ($\boldsymbol{W/B}$) of 0.42, a cement–fly-ash–slag ratio of 7:1:2, and an equal volume replacement of NCA with RCA. In the previous exploration experiment, the pre-wetting state of RCA, expressed as the mass ratio of pre-wetting water to water required for saturated surface dry, was examined as a singular variable. The results indicated that RAC exhibited superior workability and compressive strength when the pre-wetting state was 80%. Furthermore, RAC demonstrated enhanced workability and higher compressive strength when admixed with 40% manufactured sand compared to admixtures of 0%, 20%, 60%, 80%, and 100%

manufactured sand. This study employed the fractal dimension of RCA as the sole variable to examine the impact of fractal grading characteristics of RCA on workability, mechanical property, and durability performance of RAC. Due to the higher density of NCA in comparison to RCA, the reference concrete contained marginally greater quantities of fine and coarse aggregates than the experimental concrete. The specifics of the mixture proportion are outlined in Table 6.

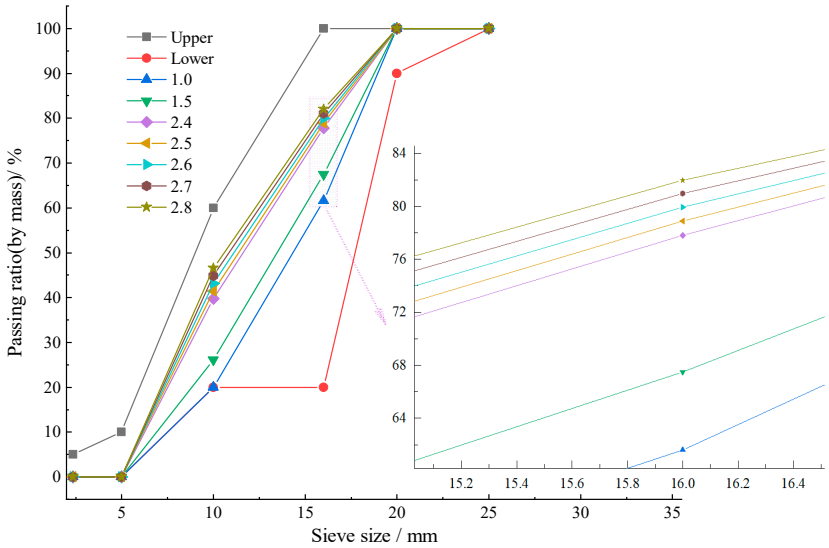

Figure 3. Aggregate grading curves with different fractal dimensions.

Table 5. Mass percentage of aggregate in each particle size range (%).

Range of Particle Diameter / Fractal Dimension	5–10 mm	10–16 mm	16–20 mm
1.0	20.00	41.60	38.40
1.5	26.12	41.37	32.51
2.4	39.75	38.06	22.19
2.5	41.42	37.46	21.12
2.6	43.11	36.83	20.06
2.7	44.82	36.15	19.03
2.8	46.50	35.40	18.10

Table 6. The mixture proportion of NAC and RAC.

Notation	MW	PW	Cement	FA	Slag	RS	MS	NCA	RCA	WR	*D*
						kg/m^3					
NAC1.0	160	0	267	38	76	445	297	1120	0	4.6	1.0
RAC1.0		39				437	291	0	1092	5.7	
RAC1.5		41									1.5
RAC2.4		43									2.4
RAC2.5		43									2.5
RAC2.6		44									2.6
RAC2.7		44									2.7
RAC2.8		44									2.8

MW represents mixing water; PW represents pre-wetting water; FA represents fly ash; RS represents river sand; MS represents manufactured sand; WR represents water reducer.

2.4. Specimens Casting and Curing

The raw material quality was evaluated based on the mix proportion outlined in Table 6 and the mass ratio of each particle size interval of coarse aggregate as specified in

Table 5. The conventional preparation process was employed to produce NAC, whereby the powder and aggregate were uniformly mixed in a mixer, followed by the addition of a mixture of superplasticizer and mixing water until all raw materials were evenly blended. The workability of the fresh concrete was then measured and cast into the test mold. While the four-times delivery approach was utilized to produce RAC, whereby RCA was adequately pre-wetted with pre-wetting water and the amalgamation was formulated using 90% of the mixing water and superplasticizer. Subsequently, cement, fly ash, slag, river sand, and manufactured sand were introduced into a SJD60 horizontal concrete mixer for dry mixing, followed by the addition of the amalgamation for wet mixing. Similarly, the pre-wetted RCA was incorporated into the mixer for mixing. Ultimately, the remaining 10% mixing water was added to the mixer, and all the raw materials were blended until a paste was formed and discharged. Following this, the workability of the RAC was evaluated and cast into the prepared molds. The detailed process of preparing the RAC specimens is illustrated in Figure 4.

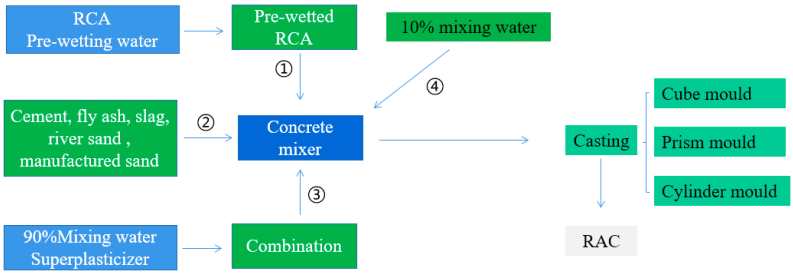

Figure 4. Preparation process of RAC.

After the initial setting, the prepared specimens were covered with a plastic film to impede moisture dissipation. After a duration of 24 h, the specimens were extracted from the molds and subsequently transferred to a standard curing chamber. The chamber was maintained at a temperature of 20 ± 3 °C and a relative humidity of 95%.

A total of 120 specimens, each with dimensions of 100 × 100 × 100 mm, were utilized to determine the cube compressive strength at 7 d, 28 d, 60 d, 90 d, and 180 d. The evaluation of concrete's resistance to chloride-ion penetration was conducted using 24 specimens with dimensions of Φ100 × 50 mm. Additionally, the carbonation resistance was evaluated by utilizing eight specimens measuring 100 × 100 × 400 mm.

2.5. Test Methods

2.5.1. Slump and Slump Flow

The compliance of the slump and slump flow with the Current Chinese National Standard "Standard for Test Method of Performance on Ordinary Fresh Concrete" was determined to assess the impact of the fractal dimension of RCA on the workability of fresh concrete.

2.5.2. Cube Compressive Strength

The cubic compressive strength of NAC and RAC were evaluated at 7 d, 28 d, 60 d, 90 d, and 180 d, in compliance with the Current Chinese National Standard "Standard for Physical and Mechanical Properties of Concrete Test Methods". The electro-hydraulic servo compression machine with a loading capacity of 3000 kN was utilized to measure the compressive strength of concrete, with a loading rate of 0.5 MPa/s.

2.5.3. Chloride Ion Penetrability

The chloride permeability of NAC and RAC was evaluated following the Current Chinese National Standard "Standard for Test Methods of Long-Term Performance and Durability of Ordinary Concrete". Concrete specimens measuring 100 × 50 mm were extracted from the standard curing chamber at 28 days of age and subjected to vacuum

preservation for water retention. The concrete's resistance to chloride ion penetration was then determined by measuring the total charge passed through the specimens over a test duration of 6 h.

2.5.4. Carbonation Depth

The accelerated carbonation experiment was utilized to measure the carbonation depth of NAC and RAC. In order to mitigate the impact of individual variability of specimens on the test results, the carbonation depth of the same concrete prism was assessed within a carbonation box for 7, 14, 28, 56, 84, and 120 days. After measuring the depth of carbonization, the specimen's cross-section was sealed with paraffin wax and placed in a container to continue carbonization until the next testing period. The truncation thickness for each break test was set at 50 mm.

3. Results and Discussion

3.1. Workability

The height difference between the height of the slump cone and the position of the fresh concrete mixture is defined as the slump value, while the slump flow is the arithmetical mean of the maximum diameter of the mixture and its diameter in the vertical direction. Figure 5 illustrates the slump and slump flow values of the concrete mixtures. It can be observed that the slump and slump flow of RAC decrease with the increase of fractal dimension. As ***D*** increases from 1.0 to 2.8, the slump and slump flow decrease from 225 mm and 550 mm to 150 mm and 375 mm, respectively, indicating a decrease of 93.3% and 31.2%, respectively. The corresponding ratio of slump flow to slump for ***D*** values of 1.0, 1.5, 2.4, 2.5, 2.6, 2.7, and 2.8 are 2.44, 2.32, 2.35, 2.34, 2.47, 2.39, and 2.50, respectively, with a small fluctuation range. This indicates that the slump and slump flow can effectively be evaluated for the workability of fresh RAC. There may be two main reasons why the workability of RAC decreases with increasing ***D***, as the other conditions are the same. First, the larger the ***D***, the higher the content of the small- and medium-size particles (5–10 mm) in the coarse aggregate gradation, and the larger the total surface area of RCA. The thickness of the cement paste wrapped around the surface of the aggregate will be decreased under the condition that the cement paste content remains the same. It reduced the lubrication of cement paste on aggregate and increased the resistance between the aggregates. The fluidity of the mixture is reduced, which is manifested by the reduction of the slump and slump flow. A higher value of ***D*** in the gradation system indicates a greater content of smaller particles in the aggregate, leading to a higher content of old mortar in RCA. This results in increased water absorption, ultimately reducing the amount of mixing water available.

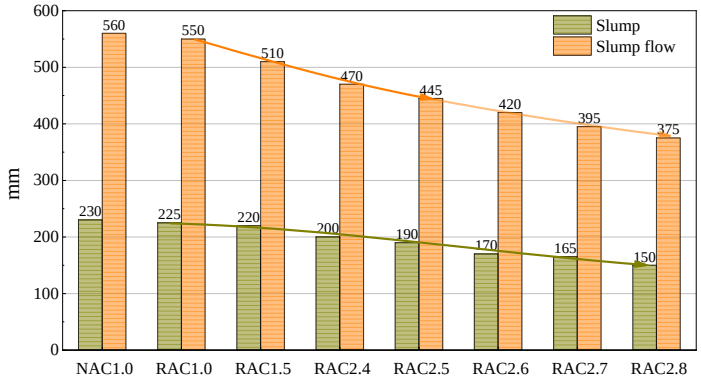

Figure 5. Slump and slump flow of NAC and RAC.

3.2. Compressive Strength and the Effect of Fractal Dimension

Figure 6 displays the cubic compressive strength development of different materials at 7, 28, 60, 90, and 180 days. The results suggest that the compressive strength of concrete

decreases when RCA completely replaces NCA. However, the compressive strength of RAC with varying ***D*** values is not consistent. Specifically, as ***D*** increases from 1.0 to 2.8, the RAC compressive strength initially increases and then decreases. Table 7 provides the standard deviations of compressive strength for different concrete types at various curing ages. The results indicate that the mean standard deviations of RAC2.4, RAC2.5, and RAC2.6 are 0.70, 0.94, and 0.90, respectively. These values are significantly lower than the mean standard deviations of other RACs and slightly lower than that of NAC. This indicates that the compressive strength of RAC remains more consistent when the aggregate fractal dimension is 2.4, 2.5, and 2.6. Through the normality test conducted on the compressive strength of NAC and RACs, it was found that, at the 0.05 significance level, the compressive strength significantly follows a normal distribution. A one-way analysis of variance (ANOVA) was conducted on the 90-day compressive strength, revealing a significant correlation between the compressive strength values of RAC and NAC. Additionally, a box plot depicting this relationship is presented in Figure 7. The solid diamonds within the boxes represent experimental scatters while the hollow rectangles represent the mean values. Figure 7 illustrates that the mean compressive strength fluctuates around the median value. The range of RAC2.5 is smaller than that of NAC, and the test values are closer to the mean value. These observations, along with the results from Table 7, collectively indicate the relatively stable nature of the compressive strength values for RAC2.5.

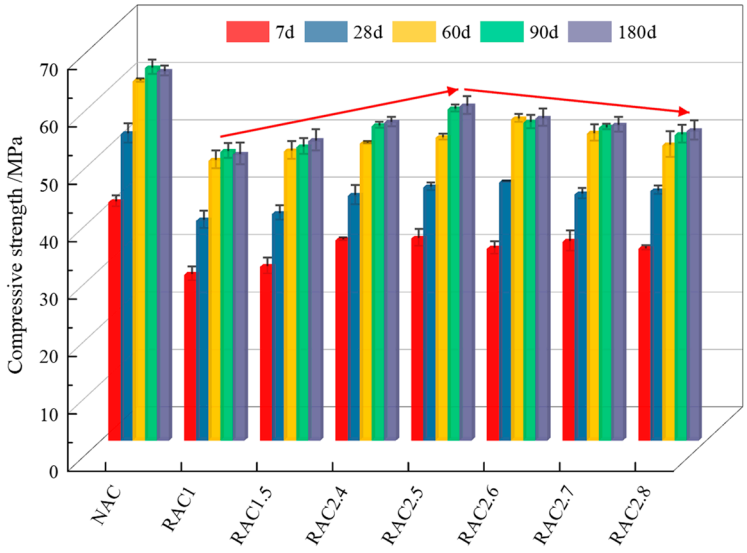

Figure 6. The compressive strength of NAC and RAC at various curing ages.

Table 7. The standard deviations of compressive strength for NAC and RAC(MPa).

Notation \ Curing Age	7 d	28 d	60 d	90 d	180 d	Mean Value
NAC1.0	0.92	1.67	0.31	1.24	0.86	1.00
RAC1.0	1.22	1.51	1.52	1.28	1.91	1.49
RAC1.5	1.37	1.25	1.56	1.35	1.87	1.48
RAC2.4	0.26	1.67	0.22	0.53	0.84	0.70
RAC2.5	1.45	0.62	0.50	0.62	1.51	0.94
RAC2.6	1.06	0.09	0.68	1.16	1.52	0.90
RAC2.7	1.77	0.90	1.41	0.45	1.29	1.16
RAC2.8	0.39	0.74	2.24	1.53	1.68	1.32

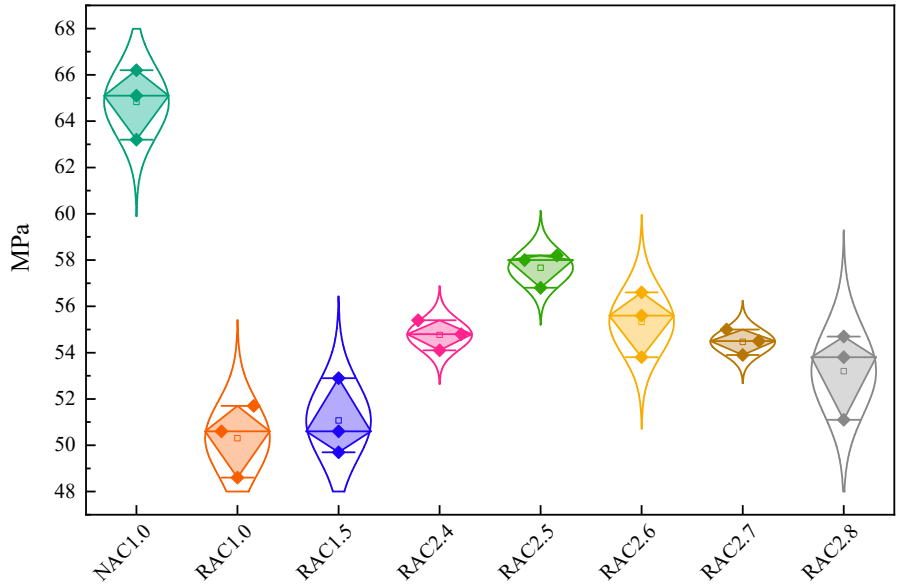

Figure 7. The box plot of compressive strength at 90 d.

The coarse aggregate gradation used in construction engineering is closer to the gradation with a fractal dimension of 1.0. The compressive strength difference and enhancement rate of NAC1.5, RAC2.4, RAC2.5, RAC2.6, RAC2.7, and RAC2.8 compared with RAC1.0 are given in Table 8. It can be found that the RAC with an aggregate fractal dimension from 2.4 to 2.8 has a large increase, up to 8.4 MPa, and the largest enhancement rate is 16.7%.

Table 8. Difference strength and enhancement rate of RACs compared to RAC1.0.

Curing Days	Difference Strength/MPa						Enhancement Rate/%					
	RAC1.5	RAC2.4	RAC2.5	RAC2.6	RAC2.7	RAC2.8	RAC1.5	RAC2.4	RAC2.5	RAC2.6	RAC2.7	RAC2.8
7 d	0.5	2.6	2.9	1.1	2.3	1.1	1.5	8.0	9.0	3.4	7.1	3.4
28 d	0.6	2.0	3.5	4.3	2.3	2.8	1.5	4.9	8.6	10.6	5.7	6.9
60 d	0.6	2.8	3.8	7.0	4.5	2.5	1.2	5.7	7.8	14.3	9.2	5.1
90 d	0.7	4.2	7.1	4.7	3.9	2.6	1.4	8.3	14.0	9.3	7.7	5.1
180 d	1.1	5.3	8.4	5.7	4.4	3.5	2.2	10.5	16.7	11.3	8.7	6.9

The difference in compressive strength between NAC and RAC is 4~14 MPa, as shown in Figure 8, indicating that RAC has a lower strength grade (1~3) than NAC with the same water–binder ratio. Additionally, Figure 8 shows that, as the fractal dimension of the aggregate increases, the compressive strength difference of the concrete initially decreases and then increases. The compressive strength difference decreases slowly when D is less than 2.4, but it increases significantly when D is greater than 2.6. In addition, the mean curve of the difference in compressive strength at 7 d, 28 d, 60 d, 90 d, and 180 d also demonstrates that the threshold value of the fractal dimension of RAC is between 2.5 and 2.6, which means that an optimal value exists between 2.5 and 2.6, resulting in the highest compressive strength of RAC.

The results shown in Figure 9 were obtained by normalizing the compressive strength of concrete using Formula (13). It is observed that the normalized strength (y) increases steadily with the growth of curing age, showing an "upward convex" growth trend. The strength of NAC remained consistent after 60 days, whereas the strength of RAC stabilized after 90 days. Additionally, the normalized strength of RAC is higher compared to that of NAC. The possible reason for this situation is that, along with the cement hydration and the pozzolanic effect of mineral admixture, the old mortar in the RCA underwent a chemical reaction and produced a small amount of C-S-H gel.

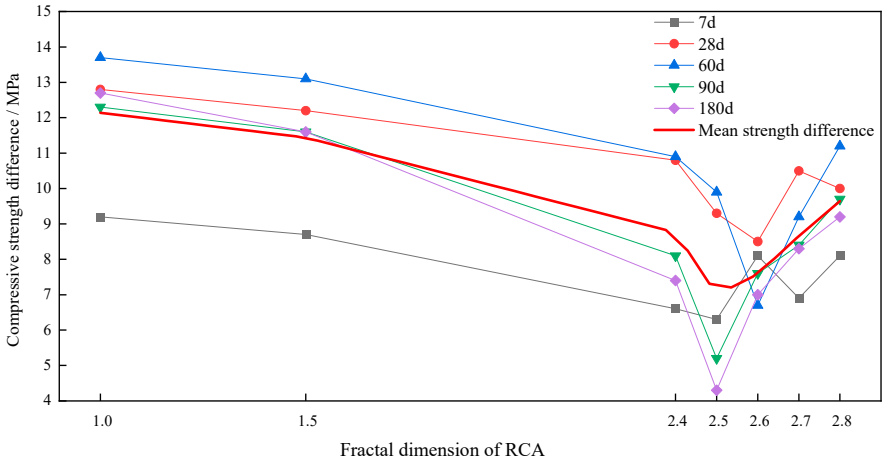

Figure 8. Difference in cube compressive strength of NAC and RAC.

$$y = \frac{f_{cu,\mathrm{d}}}{f_{cu,7}} \tag{13}$$

where $f_{cu,d}$ is the cube compressive strength at d days, MPa, and $f_{cu,7}$ is the 7 d cube compressive strength, MPa.

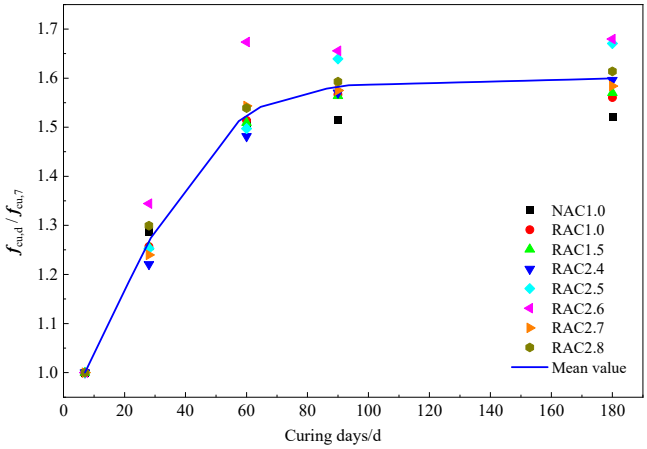

Figure 9. The relationship between normalized strength and curing days.

The reduction rate (η) of RAC compressive strength is calculated by dividing the difference in strength between NAC and RAC by the strength of NAC:

$$\eta = \frac{f_{cu,\mathrm{NAC}} - f_{cu,D}}{f_{cu,\mathrm{NAC}}} \tag{14}$$

where $f_{cu,NAC}$ and $f_{cu,D}$ are the compressive strength of NAC and RAC with a fractal dimension of D, respectively.

The relationship between η of compressive strength and curing age is presented in Figure 10. It is obvious that, as the age increases, η initially increases, then decreases, and finally stabilizes. Additionally, the η at 60 d, 90 d, and 180 d was less than that at 28 d. This illustrates that the late strength development of RAC is more consistent than that of NAC. This may be due to the increased alkalinity of calcium hydroxide in the RCA. Compared with NAC, there is more calcium hydroxide reacting with the silica when the cement content is the same, thus showing the phenomenon of "although the compressive strength of RAC is lower than that of NAC, the reduction rate decreases with curing age".

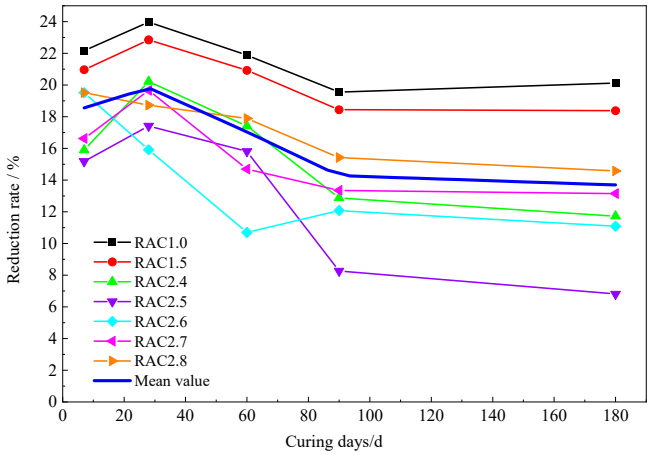

Figure 10. The reduction rate of RAC compressive strength compared to that of NAC.

The above phenomenon can be explained by the theory of high packing and the pozzolanic effect of old mortar. The packing density of a given volume of bone material is closely related to the size distribution of the aggregate particles. The particle size distribution of different fractal dimensions of aggregate is different (as shown in Figure 3). Therefore, even if aggregates with the same mass are stacked into a system of the same apparent volume, the internal void ratio is different, that is, the compactness degree of the system is different. Theoretically, there is an optimal fractal dimension value (threshold), which makes the aggregate system the most compact, and its compactness degree can be characterized by porosity or compacted bulk density. The threshold is stable for the same NCA with relatively uniform texture, but it may fluctuate in a small range for complex RCA. The complexity of RCA mainly comes from the composition and content of old mortar. According to Akbarnezhad [39], there is a negative correlation between the compressive strength of RAC and the old mortar content. This means that, as the old mortar content increases, the compressive strength of RAC decreases. It is clear that RCA systems with the same quality and different fractal dimensions usually have different old mortar contents. Since it is difficult to ensure that the mix is uniform in each specimen during the casting process, there is also a slight difference in the old mortar content between specimens prepared with the same fractal dimension aggregate, which can explain why the strength of RAC2.5 at 28 d and 60 d is lower than that of RAC2.6 while the strength at other curing ages is higher than that of RAC2.6.

In Figure 11, the difference in strength between the curing ages is shown. The results indicate that the compressive strength of NAC and RAC increases by 8–12 MPa at 28 d compared to 7 d, and that of 60 d compared to 28 d. However, the compressive strength increases after 60 d are limited, except for RAC 2.5, which shows an increase by 5 MPa at 90 d compared to 60 d. The strength of other concretes remains within 2 MPa. This suggests that the pozzolanic effect of fly ash and slag mainly occurs before 60 d. Liu et al. [40] discovered that the old mortar in the RCA contains SiO_2 and Al_2O_3, and also has some pozzolanic effect. Truly, RAC1.0 and NAC1.5 with fractal dimensions of 1.0 and 1.5 contain less old mortar than other groups, which is one of the reasons why the compressive strength is lower than other RACs. It is obvious that the compressive strength of concrete is a comprehensive reflection of many factors, such as cement hydration, the accumulation degree of aggregate, and the pozzolanic effect. Although the old mortar content in RAC2.7 and RAC2.8 is higher than that in RAC2.5 and RAC2.6, and the pozzolanic effect of the old mortar in RAC2.7 and RAC2.8 is more active, the degree of compact accumulation is weaker and the area of the ITZ is larger, so the compressive strength of RAC2.7 and RAC2.8 is lower than that of RAC2.5 and RAC2.6.

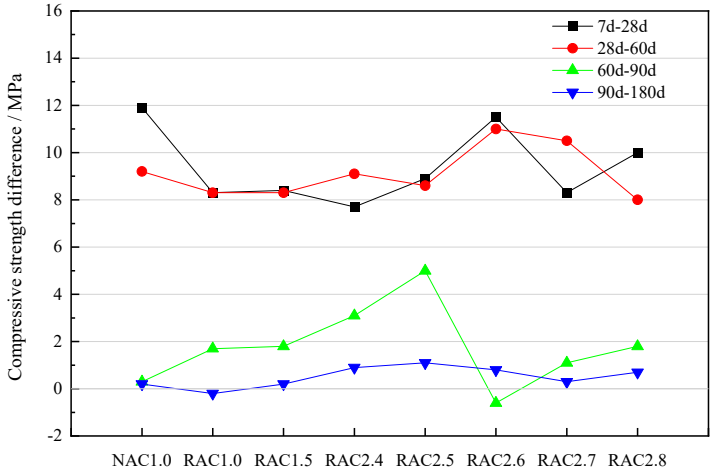

Figure 11. Difference in cube compressive strength of each curing day.

The compressive strength of each age(t) and different aggregate fractal dimension (D) were analyzed through surface regression analysis (Figure 12) to obtain the RAC compressive strength model, as shown in Formula (15). The R^2 value fitted by the above formula is 0.97, and the residual error is 2.37, with good reliability of the compressive strength model.

$$f_{cu}(D,t) = f_{cu}(1.0,28) - 2.9D^2 + 13.3D + 4.3e^{-\frac{(D-2.547)^2}{2*0.035^2}} - 27.4e^{-\frac{t}{28}} \quad (15)$$

where $f_{cu,}$ (1.0, 28) is the compressive strength of RAC cured for 28 d with the fractal dimension of 1.0, which is 40.2 MPa in this study.

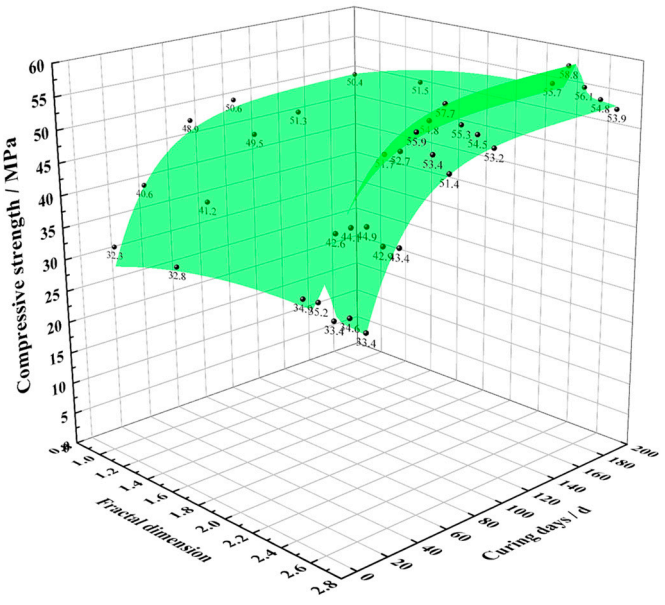

Figure 12. The compressive strength of RAC versus the fractal dimension of RCA and curing days.

Based on the strength model, the partial derivative is calculated for D.

$$\frac{\partial f_{cu}(D,t)}{\partial D} = 13.3 - 5.8D - 15093.9(D - 2.547)e^{-\frac{(D-2.547)^2}{2*0.035^2}} \quad (16)$$

Letting $\frac{\partial f_{cu}(D,t)}{\partial D} = 0$, the numerical solution of D can be obtained as 2.547, and the mass percentage of each particle size interval is shown in Table 9.

Table 9. The sieve residue rate of RCA with a fractal dimension of 2.547.

Rang of Particle Diameter/mm	5–10	10–16	16–20
Sieve residual rate/%	42.21	37.17	20.62

3.3. Chloride Penetrability

Figure 13 displays the results of the resistance to chloride ion permeation (RCP) of NAC and RAC after 28 days of standard curing. The total charge passed (TCP) for RAC1.0, RAC1.5, RAC2.4, RAC2.7, and RAC2.8 increased by 13.4%, 9.8%, 1.9%, 2.9%, and 5.5%, respectively, when compared with NAC1.0. However, RAC2.5 and RAC2.6 reduced by 1.7% and 4.6%, respectively. Similarly, the effect of RCA fractal dimension on the RCP of RAC is consistent with the effect of compressive strength, i.e., as the fractal dimension increases, the RCP of RAC initially increases and then decreases. Specifically, the TCP of NAC1.5, RAC2.4, RAC2.5, RAC2.6, RAC2.7, and RAC2.8 were 3.3%, 10.1%, 13.3%, 15.5%, 9.3%, and 7.0%, respectively, lower than that of RAC1.0. It suggested that the TCP of RAC can be reduced, even lower than that of NAC, by adjusting the gradation fractal dimension of RCA. The normality test also demonstrates the significant normal distribution of the TCP data, as verified by the one-way ANOVA results shown in Figure 14. Figure 14 reveals that the scatter range of data for RAC2.5 is the smallest, indicating a higher degree of consistency within the dataset. However, in the case of RAC2.6, a single data point's small value leads to a larger range and variance. According to the Current Chinese National Standard "Standard for Test Methods of Long-Term Performance and Durability of Ordinary Concrete", when the difference between one TCP value and the median exceeds 15% of the median, the arithmetic mean of the remaining two TCP values is taken as the measured value. Consequently, the TCP value for RAC2.6 is not the mean of the three specimens, while the concrete's TCP value is the mean of the three specimens. This elucidates that the test results are relatively favorable. According to the analysis results, when $\boldsymbol{D}$ is 2.5, the TCP standard deviation for RAC is at its minimum and the RCP of RAC2.5 is also more stable, as observed with the compressive strength. The chloride penetrability and the RCP of RAC were evaluated concerning ASTMC 1202 and Chinese national standard JGJ/T193-2009, and the results indicate that both were low and good, respectively.

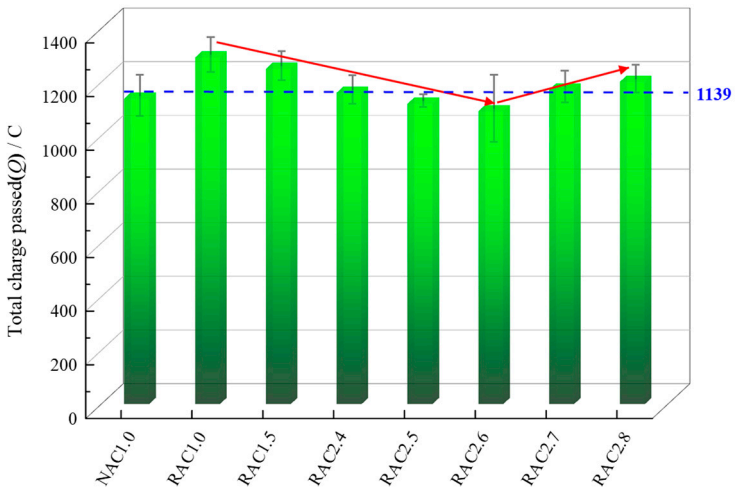

Figure 13. The total charge passed through NAC and RAC with various fractal dimensions.

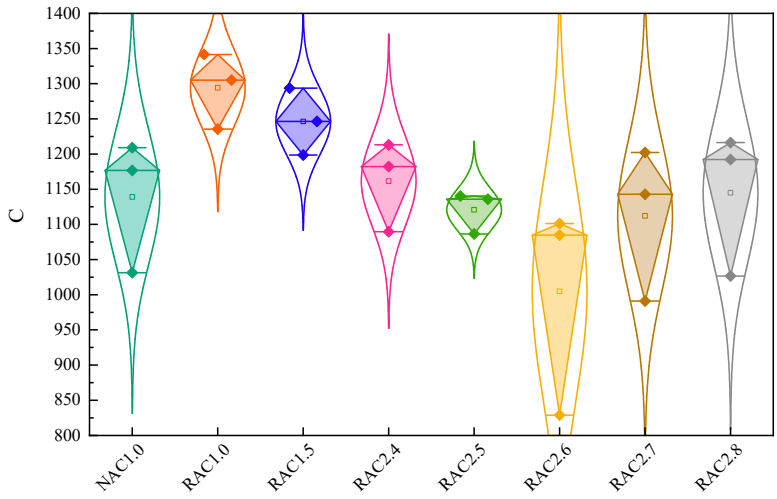

Figure 14. The statistic analysis of total charge passed through NAC and RAC with various fractal dimensions.

The results have shown that RCA has minimal impact on the RCP of concrete. For instance, the TCP of RAC1.0 is only 13.43% higher compared to NAC1.0, while the compressive strength of RAC1.0 is about 24% lower than that of NAC1.0. The reason for this phenomenon is that RCA is sufficiently covered by new mortar, and the micropores of old mortar inside RCA are blocked. This is different from the cracks formation and expansion of concrete during loading. The chloride ion penetration performance test does not involve the accumulation of internal damage in concrete under loading, and the chloride ions may mainly diffuse along the edges of the new interface transition zone or the micro-cracks therein; therefore, the plugging effect of the new mortar plays a better role.

Due to the higher water absorption of RCA, the interfacial transition zone (ITZ) between RCA and the new mortar will contain more free water. This increases the local water–binder ratio and reduces the compactness of the area. As a result, RAC and NAC, with the same fractal dimension, exhibit a weaker RCP of RAC compared to NAC. These findings are consistent with the results reported by Kou and Poon et al. [11,23]. On the other hand, according to the theory of high packing, there exists an optimal fractal dimension in an aggregated system that results in a tight packing state. The closer the value of the fractal dimension is to this optimal value, the closer the aggregated system is to achieving the tightest packing state. Thereby, the new ITZ will become narrower and more tortuous, so the diffusion path of chloride ions is lengthier and more complex, and its ability to resist chloride ion penetration will be stronger. This can reasonably explain the experimental results. The possible paths of chloride ion penetration and diffusion in concrete with an aggregate fractal dimension of 1.0 and 2.5 are given in Figure 15. The TCP by RAC2.5 and RAC2.6 is less than that of NAC1.0 due to the above two reasons, which is that the tight accumulation effect is greater than the weakening effect of ITZ caused by RCA.

3.4. Carbonation Resistance

The carbonation depths measured after NAC and RAC reached the set carbonation time are shown in Figure 16. It was found that the carbonization depth of RAC1.0 after 7 d, 14 d, 28 d, 56 d, and 112 d of accelerated carbonization increased by 64.7%, 65.0%, 66.7%, 72.0%, and 51.2% respectively, compared with that of NAC1.0. This indicates that the carbonation depth of RAC1.0 is approximately 1.7 times greater than that of NAC1.0 for $\boldsymbol{D}$ of 1.0, which is in agreement with the results of Zhu and Kou [23]. Additionally, the carbonation depth of RAC gradually decreases with the increase of $\boldsymbol{D}$, which is consistent with the carbonization depth of RAC characterized by microporous fractal dimension in Tang et al. [41]. This consistency underscores that aggregate fractal gradation is a fundamental characteristic of RAC. Figure 17 represents the box plot obtained from the

one-way ANOVA on the carbonation depth of NAC and RACs at 112 days. The results of the variance analysis indicate a significant difference in population means at the 0.05 significance level. Observing Figure 17, it becomes apparent that the mean and median of the 112-day carbonation depth are nearly equal. Moreover, with the exception of NAC's range of 1 mm, the ranges for the RACs are 1.5 mm. This suggests that the incorporation of RCA leads to a reduction in the stability of concrete's carbonation resistance. The decrease in carbonation depths for RAC1.5, RAC2.4, RAC2.5, RAC2.6, RAC2.7, and RAC2.8 compared with RAC1.0 are shown in Figure 18**,** and it can be seen that $\boldsymbol{D} \in [2.4,2.7]$, the decrease rate of carbonization depth, increases rapidly while $\boldsymbol{D}$ is relatively flat outside this range.

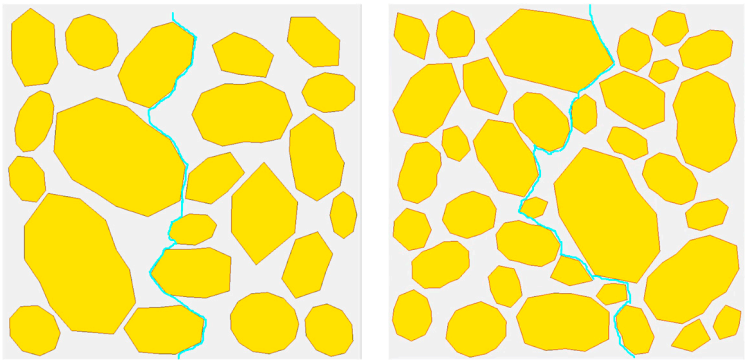

(**a**) $\boldsymbol{D}$ = 1.0 (**b**) $\boldsymbol{D}$ = 2.5

Figure 15. The possible paths of chloride ion penetration and diffusion in concrete with an aggregate fractal dimension of 1.0 and 2.5.

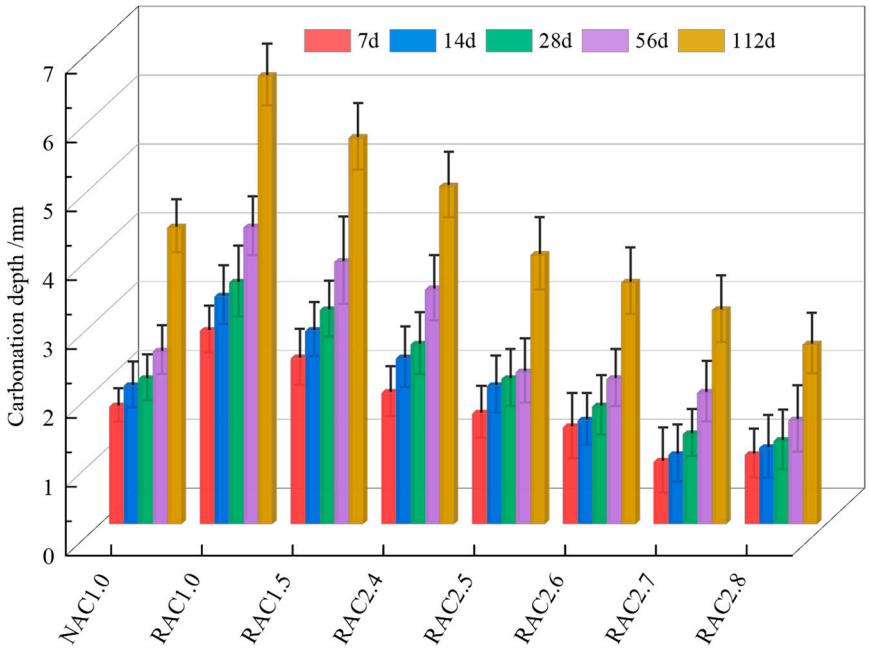

Figure 16. The carbonation depth of NAC and RAC.

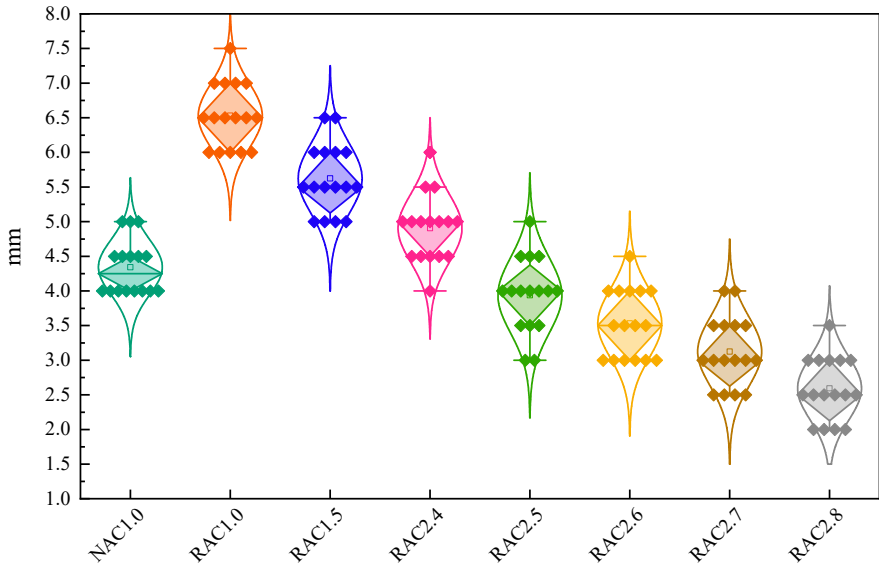

Figure 17. The box plot of carbonation depth at 112 d.

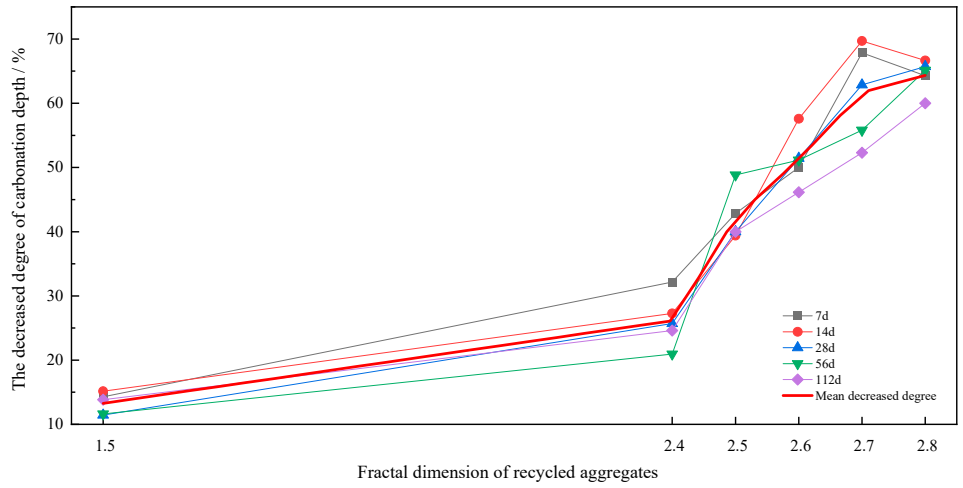

Figure 18. The carbonation depth of NAC and RAC.

It is worth noting that the carbonation depth of RAC2.5 is comparable to NAC1.0, while the carbonation depth of RAC2.6, RAC2.7, and RAC2.8 is smaller than that of NAC1.0. The phenomenon may be attributed to the fact that the old mortar contains un-hydrated cement particles and calcium hydroxide, which increases the alkalinity of RAC, making its total alkalinity higher than that of NAC with the same amount of cement. It is clear that the larger ***D*** is, the more 5–10 mm particles there are, and most of the 5–10 mm RCA particles are pure mortar particles, so the more old mortar content there is, the higher the alkalinity of RAC. It is widely acknowledged that the internal alkalinity of concrete is a key factor in determining its resistance to carbonation. As a result, with an increase in ***D***, the carbonation depth of RAC is observed to decrease.

Some particles of RCA have undergone natural carbonation before mixing the concrete, and this characteristic significantly affects the carbonation resistance of RAC. Figure 19 displays four types of special areas for RAC carbonization. ① is RCA particles that reduce the carbonization depth of concrete, and these RCA particles do not undergo natural carbonization. ② is RCA particles located at the edge of RAC, and all or most of these particles have been completely carbonized before mixing. Due to the porous characteristics of RCA, the carbonization speed will be accelerated when the outer mortar matrix is carbonized, and finally, the local carbonization depth will be increased. Both cases are also

described by Leemann and Loser [42]. Therefore, the carbonization interface of RAC is more tortuous and complex, compared with the relatively flat carbonization interface of NAC. Particles ③ and ④ are located within the RCA and undergo natural carbonization on the RCA surface and the RCA as a whole, respectively. These processes have a relatively small impact on the carbonization performance of the RAC, just as other similar studies related to the RA-based concrete [43–47].

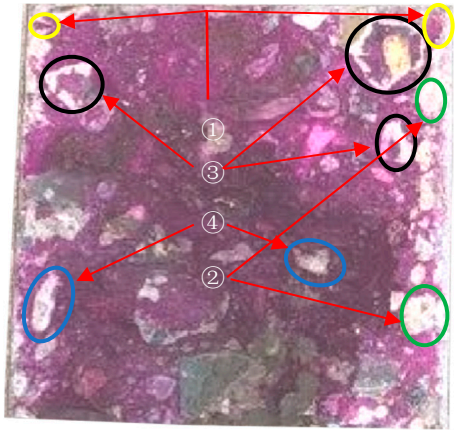

Figure 19. Four types of special areas for RAC carbonization.

4. Conclusions

The main conclusions are drawn as follows.

- With the increase of $\boldsymbol{D}$, the slump and slump flow of RAC are reduced. However, the liquidity loss can be compensated by adding suitable pre-wetted water and water-reducing agent.
- The RAC strength model, which takes into account the variables of $\boldsymbol{D}$ and curing age, is formulated through regression analysis. The optimal fractal dimension is identified as 2.547, and the corresponding mass percentages for each particle size are determined.
- In comparison to the compressive strength, RCA has a relatively less detrimental impact on the chloride ion permeation. The chloride ion penetration of RCA ($\boldsymbol{D}$ = 2.5) relative to RCA ($\boldsymbol{D}$ = 1) is reduced by 13.3%.
- The carbonation depth of RAC ($\boldsymbol{D}$ = 1) is 1.7 times greater than that of NAC. The carbonation depth of RAC ($\boldsymbol{D}$ = 2.5) is comparable to that of NAC ($\boldsymbol{D}$ = 1.0), while the carbonation depths of RAC ($\boldsymbol{D}$ = 2.6), RAC ($\boldsymbol{D}$ = 2.7), and RAC ($\boldsymbol{D}$ = 2.8) are smaller than that of NAC ($\boldsymbol{D}$ = 1).

Author Contributions: Conceptualization, C.-Q.Q.; methodology, X.-F.C.; writing—original draft and editing, C.-Q.Q.; experiment, C.-Q.Q. and W.-Z.C.; supervision, C.-J.J.; project administration, C.-J.J.; software, X.-F.C.; writing—review and editing, R.L. and X.-F.C.; funding acquisition, C.-J.J. and Z.-C.X. All authors have read and agreed to the published version of the manuscript.

Funding: The work described in this paper was supported by grants from the National Natural Science Foundation of China (Project No. 52078148 and 52108125), Characteristic Innovation Project of Colleges and Universities in Guangdong Province (Project No. 2019KTSCX102), Basic Research Program (Municipality-University joint fund) of Science and Technology Bureau of Guangzhou (Project No. SL2023A03J00880). [Special Research Projects in Key Areas for Colleges and Universities in Guangdong Province] grant number [No. 2021ZDZX4009], [Natssural Science Foundation of Guangdong Province, China] grant number [No. 2022A1515010038], [Tertiary Education Scientific Research Project of Guangzhou Municipal Education Bureau] grant number [No. 202235263], [Zhuhai Municipal Science and Technology Planning Project in the Field of Social Development] grant number [No. ZH22036201210032PWC], [Intramural Research Program of Guangzhou University] grant number [No. RC2023035]. This project was also financially supported by the [China Postdoctoral Science Foundation] grant number [No. 2022M713666], [Natural Science Foundation of Fujian] grant

number [No. 2023J01999], and [Engineering Research Center of Disaster Prevention and Mitigation of Southeast Coastal Engineering Structures of Fujian Province University] grant number [No. 2022001].

Institutional Review Board Statement: Not applicable.

Informed Consent Statement: Not applicable.

Data Availability Statement: Data sharing not available.

Acknowledgments: Special thanks to the 'Testing Technology Center for Materials and Devices of Tsinghua Shenzhen International Graduate School' for providing testing-related services.

Conflicts of Interest: The authors declare no conflict of interest.

References

1. Wang, B.; Yan, L.; Fu, Q.; Kasal, B. A Comprehensive Review on Recycled Aggregate and Recycled Aggregate Concrete. *Resour. Conserv. Recycl.* **2021**, *171*, 105565. [CrossRef]
2. Gao, S.; Li, Q.Y.; Luo, J.L. Fractal characteristic of recycled aggregate and its influence on the physical property of recycled aggregate concrete. *Rev. Adv. Mater. Sci.* **2021**, *60*, 663–677. [CrossRef]
3. Tang, Y.C.; Zhu, M.; Chen, Z.; Wu, C.J.; Li, C.; Li, L.J. Seismic performance evaluation of recycled aggregate concrete-filled steel tubular columns with field strain detected via a novel mark-free vision method. *Structures* **2022**, *37*, 426–441. [CrossRef]
4. Xiong, Z.; Wei, W.; Liu, F.; Cui, C.; Zeng, Y. Bond behavior of recycled aggregate concrete with basalt fibre-reinforced polymer bars. *Compos. Struct.* **2021**, *256*, 1–16. [CrossRef]
5. Xu, F.; Wang, S.; Li, T.; Liu, B.; Li, B.B.; Zhou, Y. Mechanical properties and pore structure of recycled aggregate concrete made with iron ore tailings and polypropylene fibers. *J. Build. Eng.* **2020**, *33*, 101572. [CrossRef]
6. Bao, J.W.; Li, S.G.; Zhang, P.; Ding, X.Y.; Xue, S.B.; Cui, Y.F.; Zhao, T.J. Influence of the incorporation of recycled coarse aggregate on water absorption and chloride penetration into concrete. *Constr. Build. Mater.* **2020**, *239*, 117845. [CrossRef]
7. Silva, R.V.; Brito, J.D.; Dhir, R.K. Properties and composition of recycled aggregates from construction and demolition waste suitable for concrete production. *Constr. Build. Mater.* **2014**, *65*, 201–217. [CrossRef]
8. Ryu, H.S.; Shin, S.H.; Lim, S. Evaluation on the Surface Modification of Recycled Fine Aggregates in Aqueous H2SiF6 Solution. *Int. J. Concr. Struct. Mater.* **2018**, *12*, 237–247. [CrossRef]
9. Tang, W.C.; Khavarian, M.; Yousefi, A.; Chan, R.W.K.; Cui, H.Z. Influence of Surface Treatment of Recycled Aggregates on Mechanical Properties and Bond Strength of Self-Compacting Concrete. *Sustainability* **2019**, *11*, 4182. [CrossRef]
10. Kou, S.C.; Poon, C.S. Properties of concrete prepared with PVA-impregnated recycled concrete aggregates. *Cem. Concr. Compos.* **2010**, *32*, 649–654. [CrossRef]
11. Zhu, Y.G.; Kou, S.C.; Poon, C.S.; Dai, J.G.; Li, Q.Y. Influence of silane-based water repellent on the durability properties of recycled aggregate concrete. *Cem. Concr. Compos.* **2013**, *35*, 32–38. [CrossRef]
12. Santos, W.F.; Quattrone, M.; John, V.M.; Angulo, S.C. Roughness, wettability and water absorption of water repellent treated recycled aggregates. *Constr. Build. Mater.* **2017**, *146*, 502–513. [CrossRef]
13. Shaban, W.M.; Yang, J.; Su, H.L.; Liu, Q.F.; Tsang, D.C.W.; Wang, L.; Xie, J.H.; Li, L.J. Properties of recycled concrete aggregates strengthened by different types of pozzolan slurry. *Constr. Build. Mater.* **2019**, *216*, 632–647. [CrossRef]
14. Bui, N.K.; Satomi, T.; Takahashi, H. Mechanical properties of concrete containing 100% treated coarse recycled concrete aggregate. *Constr. Build. Mater.* **2019**, *163*, 496–507. [CrossRef]
15. Wang, J.Y.; Vandevyvere, B.; Vanhessche, S.; Schoon, J.; Boon, N.; De Belie, N. Microbial carbonate precipitation for the improvement of quality of recycled aggregates. *J. Clean. Prod.* **2017**, *156*, 355–366. [CrossRef]
16. Feng, Z.Y.; Zhao, Y.X.; Zeng, W.L.; Lu, Z.M.; Shah, S.P. Using microbial carbonate precipitation to improve the properties of recycled fine aggregate and mortar. *Constr. Build. Mater.* **2020**, *230*, 116949. [CrossRef]
17. Zhang, J.K.; Shi, C.J.; Li, Y.K.; Pan, X.Y.; Poon, C.S.; Xie, Z.B. Influence of carbonated recycled concrete aggregate on properties of cement mortar. *Constr. Build. Mater.* **2015**, *98*, 1–7. [CrossRef]
18. Zhang, J.K.; Shi, C.J.; Li, Y.K.; Pan, X.Y.; Poon, C.S.; Xie, Z.B. Performance Enhancement of Recycled Concrete Aggregates through Carbonation. *J. Mater. Civ. Eng.* **2015**, *27*, 04015029. [CrossRef]
19. Lu, B.; Shi, C.J.; Cao, Z.J.; Guo, M.Z.; Zheng, J.L. Effect of carbonated coarse recycled concrete aggregate on the properties and microstructure of recycled concrete. *J. Clean. Prod.* **2019**, *233*, 421–428. [CrossRef]
20. Pan, G.H.; Zhan, M.M.; Fu, M.H.; Wang, Y.P.; Lu, X.J. Effect of CO2 curing on demolition recycled fine aggregates enhanced by calcium hydroxide pre-soaking. *Constr. Build. Mater.* **2017**, *154*, 810–818. [CrossRef]
21. Li, W.G.; Xiao, J.Z.; Sun, Z.H.; Kawashima, S.; Shah, S.P. Interfacial transition zones in recycled aggregate concrete with different mixing approaches. *Constr. Build. Mater.* **2012**, *35*, 1045–1055. [CrossRef]
22. Kong, D.Y.; Lei, T.; Zheng, J.J.; Ma, C.C.; Jiang, J.; Jiang, J. Effect and mechanism of surface-coating pozzalanics materials around aggregate on properties and ITZ microstructure of recycled aggregate concrete. *Constr. Build. Mater.* **2010**, *24*, 701–708. [CrossRef]
23. Kou, S.C.; Poon, C.S. Enhancing the durability properties of concrete prepared with coarse recycled aggregate. *Constr. Build. Mater.* **2012**, *35*, 69–76. [CrossRef]

24. Bernal, J.; Bello, M.A. Fractal geometry and mercury porosimetry- Comparison and application of proposed models on building stones. *Appl. Surf. Sci.* **2001**, *185*, 99–107. [CrossRef]
25. Wang, L.; Guo, F.X.; Yang, H.M.; Wang, Y.; Tang, S.W. Comparison of fly ash, PVA fiber, MgO and shrinkage-reducing admixture on the frost resistance of face slab concrete via pore structural and fractal analysis. *Fractals* **2021**, *29*, 2140002. [CrossRef]
26. Wang, L.; Jin, M.M.; Guo, F.X.; Wang, Y.; Tang, S.W. Pore structural and fractal analysis of the influence of fly ash and silica fume on the mechanical property and abrasion resistance of concrete. *Fractals* **2021**, *29*, 2140003. [CrossRef]
27. Ridi, F.; Fratini, E.; Baglioni, P. Fractal structure evolution during cement hydration by differential scanning calorimetry: Effect of organic additives. *J. Phys. Chem. C* **2013**, *117*, 25478–25487. [CrossRef]
28. Lu, Q.; Qiu, Q.L.; Zheng, J.; Wang, J.Y.; Zeng, Q. Fractal dimension of concrete incorporating silica fume and its correlations to pore structure, strength and permeability. *Constr. Build. Mater.* **2019**, *228*, 116986. [CrossRef]
29. Wang, L.; Jin, M.M.; Wu, Y.H.; Zhou, Y.X.; Tang, S.W. Hydration, shrinkage, pore structure and fractal dimension of silica fume modified low heat Portland cement-based materials. *Constr. Build. Mater.* **2020**, *272*, 121952. [CrossRef]
30. Gao, Y.; Wu, K.; Yuan, Q. Limited fractal behavior in cement paste upon mercury intrusion porosimetry test: Analysis and models. *Constr. Build. Mater.* **2021**, *276*, 122231. [CrossRef]
31. Gao, Y.; Jiang, J.Y.; De Schutter, G.; Ye, G.; Sun, W. Fractal and multifractal analysis on pore structure in cement paste. *Constr. Build. Mater.* **2014**, *69*, 253–261. [CrossRef]
32. Wang, L.; Luo, R.Y.; Zhang, W.; Jin, M.M.; Tang, S.W. Effects of fineness and content of phosphorus slag on cement hydration, permeability, pore structure and fractal dimension of concrete. *Fractals* **2021**, *29*, 2140004. [CrossRef]
33. Wang, L.; Huang, Y.J.; Zhao, F.; Huo, T.T.; Chen, E.; Tang, S.W. Comparison between the influence of finely ground phosphorous slag and fly ash on frost resistance, pore structures and fractal features of hydraulic concrete. *Fractal Fract.* **2022**, *6*, 598. [CrossRef]
34. Wang, L.; Zhou, S.H.; Shi, Y.; Huang, Y.J.; Zhao, F.; Huo, T.T.; Tang, S.W. The Influence of fly ash dosages on the permeability, pore structure and fractal features of face slab concrete. *Fractal Fract.* **2022**, *6*, 476. [CrossRef]
35. Felekoglu, B. Effects of PSD and surface morphology of micro-aggregates on admixture requirement and mechanical performance of micro-concrete. *Cem. Concr. Compos.* **2007**, *29*, 481–489. [CrossRef]
36. Lavergne, F.; Sab, K.; Sanahuja, J.; Bornert, M.; Toulemonde, C. Investigation of the effect of aggregates' morphology on concrete creep properties by numerical simulations. *Cem. Concr. Res.* **2015**, *71*, 14–28. [CrossRef]
37. Belmokaddem, M.; Mahi, A.; Senhadji, Y.; Pekmezci, B.Y. Mechanical and physical properties and morphology of concrete containing plastic waste as aggregate. *Constr. Build. Mater.* **2020**, *257*, 119559. [CrossRef]
38. Erdem, S.; Blankson, M.A. Fractal–fracture analysis and characterization of impact-fractured surfaces in different types of concrete using digital image analysis and 3D nanomap laser profilometery. *Constr. Build. Mater.* **2013**, *40*, 70–76. [CrossRef]
39. Akbarnezhad, A.; Ong, K.C.G.; Tam, C.T.; Zhang, M.H. Effects of the Parent Concrete Properties and Crushing Procedure on the Properties of Coarse Recycled Concrete Aggregates. *J. Mater. Civ. Eng.* **2013**, *25*, 1795–1802. [CrossRef]
40. Liu, T.J.; Wang, Z.Z.; Zou, D.J.; Zhou, A.; Du, J.Z. Strength enhancement of recycled aggregate pervious concrete using a cement paste redistribution method. *Cem. Concr. Res.* **2019**, *122*, 72–82. [CrossRef]
41. Tang, S.W.; He, Z.; Cai, X.H.; Cai, R.J.; Zhou, W.; Li, Z.J.; Shao, H.Y.; Wu, T.; Chen, E. Volume and surface fractal dimensions of pore structure by NAD and LT-DSC in calcium sulfoaluminate cement pastes. *Constr. Build. Mater.* **2017**, *143*, 395–418. [CrossRef]
42. Leemann, A.; Loser, R. Carbonation resistance of recycled aggregate concrete. *Constr. Build. Mater.* **2019**, *204*, 335–341. [CrossRef]
43. Jiao, C.; Ta, J.; Niu, Y.; Meng, S.; Chen, X.-F.; He, S.; Ma, R. Analysis of the Flexural Properties of Ultra-High-Performance Concrete Consisting of Hybrid Straight Steel Fibers. *Case Stud. Constr. Mater.* **2022**, *17*, e01153. [CrossRef]
44. Chen, X.-F.; Jiao, C.-J. Microstructure and Physical Properties of Concrete Containing Recycled Aggregates Pre-Treated by a Nano-Silica Soaking Method. *J. Build. Eng.* **2022**, *51*, 104363. [CrossRef]
45. Chen, X.-F.; Kou, S.-C.; Xing, F. Mechanical and Durable Properties of Chopped Basalt Fiber Reinforced Recycled Aggregate Concrete and the Mathematical Modeling. *Constr. Build. Mater.* **2021**, *298*, 123901. [CrossRef]
46. Zhou, Y.; Li, W.; Peng, Y.; Tang, S.; Wang, L.; Shi, Y.; Li, Y.; Wang, Y.; Geng, Z.; Wu, K. Hydration and Fractal Analysis on Low-Heat Portland Cement Pastes Using Thermodynamics-Based Methods. *Fractal Fract.* **2023**, *7*, 606. [CrossRef]
47. Jiao, C.-J.; Zhang, X.-C.; Chen, W.-Z.; Chen, X.-F. Mechanical Property and Dimensional Stability of Chopped Basalt Fiber-Reinforced Recycled Concrete and Modeling with Fuzzy Inference System. *Buildings* **2023**, *13*, 97. [CrossRef]